

Intermodulation spectroscopy and the nonlinear response of two-level systems in superconducting coplanar-waveguide resonators

Janka Biznárová^{1,*}, J.C. Rivera Hernández², Daniel Forchheimer³, Jonas Bylander¹, David B. Haviland², and Gustav Andersson^{1,4,†}

¹*Chalmers University of Technology, Microtechnology and Nanoscience, SE-41296 Gothenburg, Sweden*

²*Department of Applied Physics, KTH Royal Institute of Technology, SE-106 91 Stockholm, Sweden*

³*Intermodulation Products AB, Segersta, Sweden*

⁴*Pritzker School of Molecular Engineering, University of Chicago, Chicago, Illinois 60637, USA*

(Received 19 February 2024; revised 25 June 2024; accepted 26 June 2024; published 24 July 2024)

Two-level system (TLS) loss typically limits the coherence of superconducting quantum circuits. The loss induced by TLS defects is nonlinear, resulting in quality factors with a strong dependence on the circulating microwave power. We observe frequency mixing due to this nonlinearity by applying a two-tone drive to a coplanar waveguide resonator and measuring the intermodulation products using a multifrequency lock-in technique. This intermodulation spectroscopy method provides an efficient approach to characterizing TLS loss in superconducting circuits. Using harmonic balance reconstruction, we recover the nonlinear parameters of the device-TLS interaction, which are in good agreement with the standard tunneling model for TLSs.

DOI: 10.1103/PhysRevApplied.22.014063

I. INTRODUCTION

Superconducting quantum computing is facing a challenge in the relatively short coherent lifetimes of state-of-the-art qubits, currently in the submillisecond range [1–5]. A significant source of decoherence for these qubits is dielectric loss caused by parasitic two-level system (TLS) defects [6–8], whose microscopic origin is a topic of ongoing active research [9–11]. These TLSs can couple to qubits, providing a source of energy loss and parameter fluctuations, and therefore decoherence. In this paper we introduce a method for the measurement and analysis of the inherent nonlinearity of these TLSs in superconducting resonators.

Superconducting resonators are essential components of quantum processors and a good testbed for characterizing dielectric loss. In circuit quantum electrodynamics resonators are treated as linear elements, typically modeled as lumped-element *LC* oscillators. The resonator's coupling to TLS defects gives rise to a characteristic dependence of the internal quality factor Q_i on circulating power,

with a drop in Q_i at low powers where the TLS bath is not driven to saturation [12,13]. This power-dependent response makes resonators ideal for probing TLSs in a qubit's environment.

In this work we explore how the power-dependent behavior of Q_i translates to a low-power nonlinear response of the resonator. We measure this nonlinearity in a high-quality-factor coplanar waveguide (CPW) resonator, showing that it gives rise to frequency mixing, or intermodulation—a characteristic feature of nonlinear response which has been observed for TLS-induced [14] and other nonlinearities in superconducting circuits [15–17]. Intermodulation results in response at integer combinations of the applied drive frequencies, $f_{\text{IMP}} = \sum_i k_i f_i$, where f_i are drive frequencies and k_i integers. The amplitude and phase of these intermodulation products (IMPs) can be measured with large signal-to-noise ratios (SNRs) using lock-in techniques. Modeling the system as a driven harmonic oscillator with nonlinear damping due to parasitic TLSs, we reconstruct the nonlinear response of the device as a function of drive amplitude and frequency using harmonic balance analysis.

II. EXPERIMENTAL METHODS

We perform all measurements on a superconducting aluminium $\lambda/4$ CPW resonator with a resonance frequency of 4.11 GHz, capacitively coupled to a transmission line in a notch configuration. The width of the CPW center

*Contact author: jankab@chalmers.se

†Contact author: gandersson@uchicago.edu

Published by the American Physical Society under the terms of the [Creative Commons Attribution 4.0 International](#) license. Further distribution of this work must maintain attribution to the author(s) and the published article's title, journal citation, and DOI. Funded by Bibsam.

conductor is 20 μm , and the gap to ground is 10 μm . The device has no engineered nonlinear elements. All microwave measurements presented here were carried out inside a dilution refrigerator at about 10 mK using the setup outlined in Appendix B.

For the initial characterization of the resonator, we measure the S_{21} scattering parameter in transmission using a vector network analyzer and extract the relevant parameters such as Q_i and the resonance frequency f_r using the circle-fitting method [18], as detailed in Appendix D. We characterize Q_i for excitation powers ranging from the single photon level, relevant for quantum computing applications, up to 10^8 photons where we observe other, non-TLS-related loss and nonlinear mechanisms.

The average number of photons $\langle n \rangle$ circulating in the resonator is estimated using the relation [19]

$$\langle n \rangle = \frac{Z_0}{Z_r} \frac{Q_l^2}{|Q_c|} \frac{2P_{in}}{\hbar(2\pi f_r)^2}, \quad (1)$$

where Z_0 and Z_r are the characteristic impedances of the transmission line and the resonator, respectively. The power at the device input P_{in} is calculated by subtracting the input line attenuation from the measurement instrument output power. The input line attenuation was obtained via an ac-Stark shift measurement of a qubit device [20,21] in a separate experiment.

To probe nonlinearities in the device through intermodulation distortion we use a multifrequency lock-in amplifier

platform [22], where we output two drive tones separated by $\Delta = 100$ Hz [see Fig. 1(a)]. We choose this drive spacing to be significantly smaller than the power-dependent linewidth of the resonator (8–11 kHz). This choice guarantees that both the drives and the lowest-order IMPs remain well within the resonance linewidth.

We measure the response of the device to these two drive tones using a detection frequency comb demodulating the in-phase and quadrature components at frequencies spaced by $\Delta/2$. Consequently, intermodulation produces a signal at every other frequency in this comb, and the remaining detection frequencies sample the noise background. The generation of drive tones and digitization of the response are performed in the second Nyquist zone, without the use of analog mixers for frequency conversion. Odd-order IMPs (i.e., when $|k_1| + |k_2|$ is an odd number) appear as a comb of frequencies when f_c coincides with the resonance frequency f_r , as shown in Fig. 1(b). Even-order IMPs fall far outside of the resonance linewidth.

We perform intermodulation spectroscopy, stepping the detection frequency comb with the two drives in the center across a frequency range. This frequency range is centered around f_r , with a span well outside the resonance linewidth. As shown in Fig. 1(c), we detect no IMPs when the center of the comb is off-resonant. As the two drives approach f_r , we measure a clear signal at the IMP frequencies, peaking at $f_c = f_r$. The decay of the measured IMPs outside of resonance shows that the IMPs are generated in the device and are not artifacts of nonlinearities present

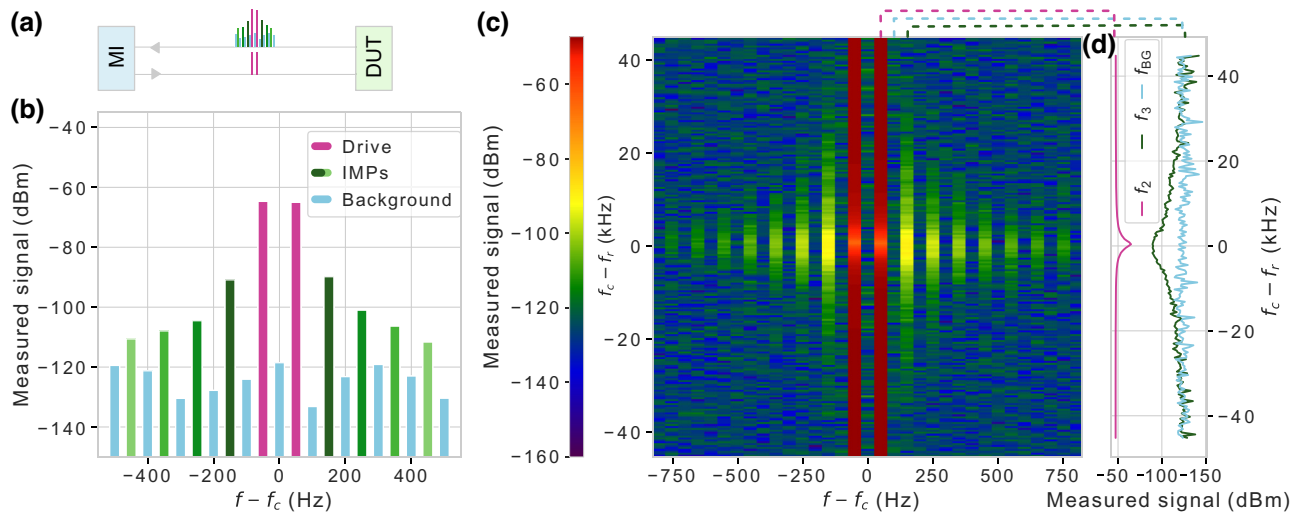


FIG. 1. Intermodulation measurements at drive powers corresponding to $\langle n \rangle = 10^3$ when on resonance. (a) A schematic of the tones generated at the output of the measurement instrumentation (MI) and the output of the device under test (DUT). (b) Intermodulation products (IMPs) measured when two drive tones are applied at resonance. The abscissa shows the detection comb frequencies f relative to the center of the detection comb $f_c = (f_1 + f_2)/2$. IMPs are detected at frequencies fulfilling the $f_{\text{IMP}} = k_1 f_1 + k_2 f_2$ condition, which falls on every other tone in this detection comb. (c) IMP power spectroscopy performed by sweeping the frequency comb depicted in (a) across a frequency spectrum centered around the resonance frequency f_r . (d) Vertical linecuts of the IMP spectroscopy data shown in (c): the device resonance is shown as a dip in the transmission of drive tone f_1 , the third IMP f_3 presents as a peak at $2f_2 - f_1$, and the background noise is shown at a frequency f_{BG} that does not correspond to any IMP. The phase response is shown in Appendix C.

elsewhere in the measurement system. Thus, we can use this intermodulation spectroscopy method to characterize nonlinearities native to our CPW resonator.

III. RESULTS

The standard resonator characterization shows the expected trend where Q_i is suppressed at low $\langle n \rangle$ due to interaction with parasitic TLSs. This observation fits the so-called standard tunneling model [23]

$$\frac{1}{Q_i} = F\delta_{\text{TLS}}^0 \frac{\tanh(hf_r/2k_B T)}{(1 + \langle n \rangle/n_c)^\beta} + \delta_0, \quad (2)$$

where $F\delta_{\text{TLS}}^0$ describes the power-dependent loss due to parasitic TLSs, with F quantifying the TLS filling factor, and δ_{TLS}^0 being the dielectric loss tangent, dependent on the density of the TLSs. The parameter n_c is the critical photon number for the saturation of the TLS bath, and the power-independent term δ_0 quantifies the other, non-TLS-related sources of loss, such as radiation or resistive losses due to quasiparticles. T , h , and k_B denote temperature, the Planck constant, and the Boltzmann constant, respectively.

In the standard tunneling model, the parameter $\beta = 0.5$ characterizes the change of Q_i with photon number. This value often fits data poorly, especially for high-quality resonators, which show a weaker power dependence [24–26]. We treat β as a fitting parameter, finding a best-fit value $\beta = 0.3$ [see Fig. 2(a)]. These deviations in β have been attributed to the spectral instability of the device-TLS system, and the interactions between different TLSs themselves, not just interactions between a TLS and the quantum circuit [27–29].

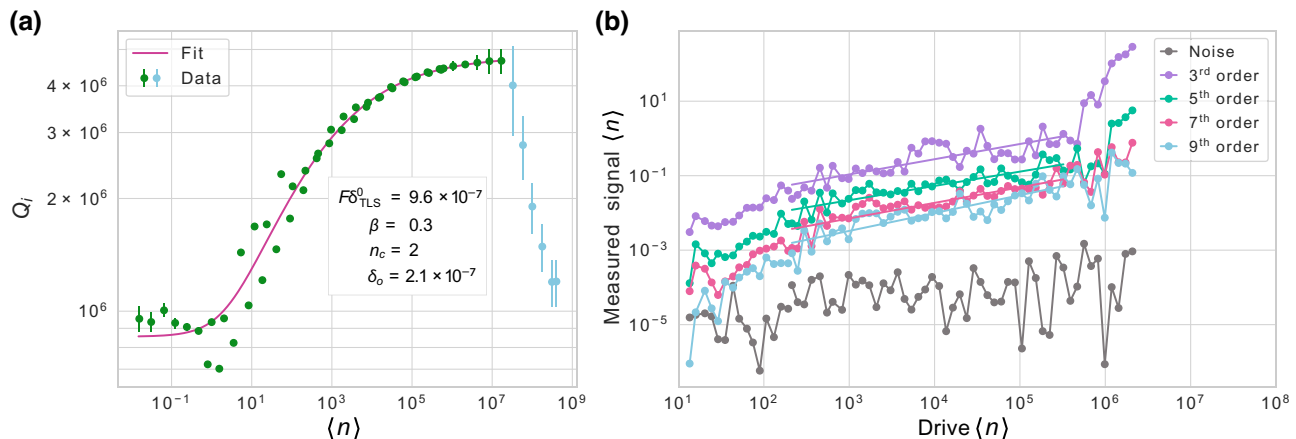


FIG. 2. (a) Internal quality factor Q_i as a function of applied power $\langle n \rangle$, fitted to Eq. (2). The high-power data plotted in blue were discarded in the fit. (b) The power of the four strongest IMPs, as well as the background noise at non-IMP frequencies, plotted as a function of applied drive power, for the case when the drive tones are applied at resonance. In the entirety of the measured power span, the signal corresponding to the two strongest IMPs measured is well above the noise floor. At drive powers exceeding about 5×10^5 photons, the dominant nonlinearity is due to kinetic inductance, and the strength of the IMPs increases rapidly. The slope of the power dependence of the data plotted on a logarithmic scale is fitted for $\langle n \rangle$ between 200 and 2×10^5 photons.

Having performed standard resonator characterization measurements, we proceed to intermodulation spectroscopy as a function of applied drive power. Figure 2(b) shows a clear signal at IMP frequencies across the entire measured power range, with a power-dependent amplitude of the measured IMPs. We identify three separate regions with different power-dependent characteristics, consistent with the observations from Fig. 2(a).

The drive powers used in this measurement exceed the critical photon number n_c . In the low-power regime where $\langle n \rangle < 200$, TLSs dominate the total loss of the resonator, and the dependence of the IMPs on power is strong with a variable slope. In the intermediate drive power regime where $\langle n \rangle \gg n_c$, the four strongest IMPs show a power-law behavior, scaling with drive power as $\langle n \rangle^k$. The fit parameters k are laid out in Table I, alongside the parameters predicted by the model in Sec. IV. We note that due to the saturation of the TLS bath, the IMPs increase more slowly than the drive amplitude (i.e., $k < 1$). The opposite is typically the case for intermodulation distortion in electronic devices [30]. At drive powers exceeding about 5×10^5 photons, the nonlinearity increases sharply, which relates to the onset of kinetic inductance effects at high input power [31,32].

These trends are consistent with the Q_i vs $\langle n \rangle$ curve shown in Fig. 2(a). Here, TLSs contribute significantly to the loss at low excitation numbers and become saturated with stronger probes. At high power, current-induced pair breaking changes the kinetic inductance and the frequency of the resonator shifts, as shown in Appendix D.

The coupling between quantum circuits and TLSs tends to fluctuate on slow timescales [29,33]. We study this effect on the measured IMPs in Fig. 3, where we repeat the same IMP spectroscopy measurement at a fixed drive power

TABLE I. Power dependence of the measured IMPs in Fig. 2(d), and of the modeled IMPs in Fig. 4, fitted to $\langle n \rangle^k \cdot 10^{y_0}$, where y_0 is the y -axis offset.

IMP order	Experimental fit k	Model fit k
3	0.41 ± 0.05	0.42
5	0.38 ± 0.04	0.43
7	0.42 ± 0.04	0.44
9	0.48 ± 0.05	0.45

level of about 10^3 photons for 25 h. Each of the individual measurements is averaged for about 5 min. We do observe seemingly random fluctuations of the measured IMPs over time in this measurement, correlated between the different orders of IMPs. The fluctuations do not extend to the measured amplitudes of the drive tones, which are stable in comparison, nor to the measured background noise. A prominent example of these fluctuations can be seen around the 7–8-h mark in Fig. 3. From this we conclude that the fluctuations are native to the nonlinearity in the device, and do not originate in the measurement setup from sources such as drifts in room-temperature electronics. The fluctuations observed Fig. 2(b) may be in part explained by the instability of the TLS spectrum that gives rise to the temporal variations shown in Fig. 3. A changing coupling between the TLS and the device over time is a typical feature of TLS interaction [34].

IV. NONLINEAR PARAMETER RECONSTRUCTION

In this section, we detail the modeling and reconstruction of the nonlinear loss due to parasitic TLSs. Our reconstruction algorithm is based on fitting the linear and nonlinear oscillator parameters to a single intermodulation spectrum by harmonic balance [35,36]. This spectrum is

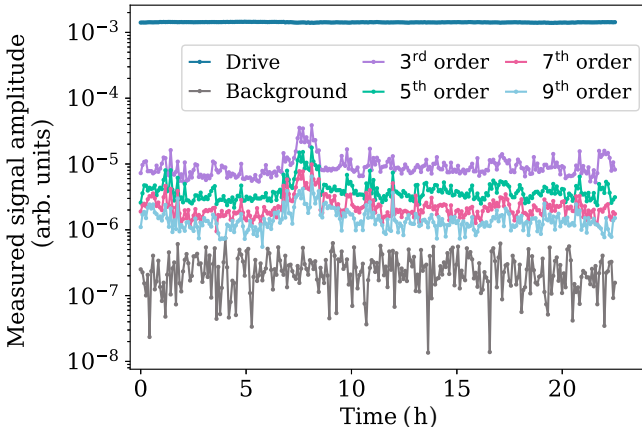


FIG. 3. IMPs measured repeatedly for 25 h, in 5-min intervals, at a constant drive power level of about 10^3 photons.

measured on resonance, with the drive power corresponding to $\langle n \rangle$ about 10^3 photons and averaged over 10 h, such as is the case in Fig. 1(a). This drive power is selected from the region of Fig. 2(a) where the power dependence of Q_i due to TLS is steep. This is so that the SNR is more favorable than the fully TLS-limited single-photon regime, but we still observe a power-dependent Q_i where the TLS bath is not fully saturated.

We model our resonator as a driven harmonic oscillator with nonlinear damping caused by parasitic TLSs. The Heisenberg-Langevin equation of motion describing the dynamics of the resonator in the rotating-wave approximation is then

$$\dot{\hat{a}} = -i\omega_0\hat{a} - \frac{\kappa_0 + \kappa_{\text{ext}}}{2}\hat{a} - \frac{\kappa_{\text{TLS}}(|a|)}{2}\hat{a} - \sqrt{\kappa_{\text{ext}}}a_{\text{in}}, \quad (3)$$

where \hat{a} and a_{in} are the time-dependent intracavity modes and the input drives respectively, ω_0 the resonant frequency, κ_0 the internal linear loss rate, κ_{ext} the external coupling to the transmission line, and $\kappa_{\text{TLS}}(|a|)$ the power-dependent loss due to parasitic TLSs. We consider a power-dependent damping of the standard form of Eq. (2), giving

$$\kappa_{\text{TLS}}(|a|)a = \frac{\kappa_{\text{TLS}}}{[1 + (|a|/a_c)^2]^\beta}, \quad (4)$$

where $\kappa_{\text{TLS}} = f_r F \delta_{\text{TLS}}^0$ represents the TLS loss rate, and $a_c^2 = n_c$ the critical photon number.

We drive the system with two tones, separated by Δ , such that the IMPs created are within the resonator's linewidth, where the sensitivity is enhanced. When the drive frequencies are periodic in some measurement time $T = 2\pi/\Delta$, and the nonlinearities and drives are sufficiently weak to avoid period doubling or chaotic behavior, the system's response is a discrete spectrum at frequencies that correspond to integer multiples of Δ . We confirm this by analyzing the system over several periods in the steady state to ensure the response remains at integer multiples of Δ .

We first solve the forward problem by numerically integrating Eq. (3) using `scipy.integrate.ode` from the SciPy library [37] to obtain the time-dependent intracavity field. The output field is then obtained using the input-output relation $\hat{a}_{\text{out}} = \sqrt{\kappa_{\text{ext}}}\hat{a} + a_{\text{in}}$. Figure 4 shows the four strongest IMPs as a function of drive power simulated with experimentally relevant parameters. For strong drives $\langle n \rangle \gg 1$, the IMP power shows a power-law scaling proportional to $\langle n \rangle^k$, with parameters k laid out in Table I. This behavior matches the experimental results shown in Fig. 2(b). We also simulate a sweep of the drive tone frequency across the resonance and analyze the power dependence of the IMPs as a function of β (see Appendix E for details).

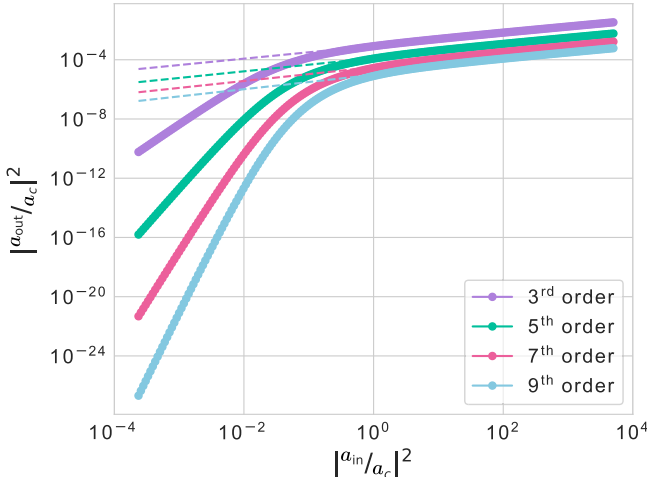


FIG. 4. Simulation of the power of the generated IMPs as a function of applied drive power. The parameters of the fit shown with dashed lines are shown in Table I.

To reconstruct the nonlinear parameters of the system, we expand the TLS damping in Eq. (4) in a power series, transforming the equation of motion to

$$\dot{\hat{a}} = -i\omega_0\hat{a} - \sum_{n=1}^N c_n |a|^{n-1} \hat{a} - \sqrt{\kappa_{\text{ext}}} a_{\text{in}}, \quad (5)$$

which is linear in the coefficients c_n . The coefficients are independent of the proposed model, allowing the application of the reconstruction algorithm to various types of nonlinearities [17,38], including unknown ones.

In the experiment we measure only a limited number of frequencies with good SNR, corresponding to the two drive tones and 14 IMPs. These frequencies, denoted as ω_k with Fourier component \hat{A}_k , represent a partial spectral response of the system. Specifically, \hat{A}_k corresponds to the intracavity field amplitude at the frequency ω_k .

By Fourier-transforming and rewriting Eq. (5) in matrix form, we arrive at an expression linear in the coefficients c_n [17],

$$\sum_l H_{kl} p_l = -A_{\text{in},k}, \quad (6)$$

where the k th row of the matrix H_{kl} is given by

$$H_k = \left(i\omega_k \hat{A}_k \ i\hat{A}_k \ \hat{A}_k \ \mathcal{F}\{|a|^2 \hat{a}\}_k \ \cdots \ \mathcal{F}\{|a|^{N-1} \hat{a}\}_k \right),$$

and p_l are the components of a vector containing the unknown parameters

$$\sqrt{\kappa_{\text{ext}}} p^T = (1 \ \omega_0 \ c_1 \ \cdots \ c_N).$$

We solve Eq. (6) by numerical pseudoinverse of the matrix H to find the best-fit vector p , which includes the

TABLE II. Reconstructed resonator parameters via fitting the standard tunneling model [Eq. (2)] and the intermodulation spectral method with harmonic balance. The third column presents results from the intermodulation spectral method with the fixed parameter $\beta = 0.3$, while in the fourth column β is left as a free parameter in the reconstruction. The error bars of the reconstructed values are computed by bootstrapping [40].

Parameters	Standard model	Harmonic balance	
		Fixed β	Free β
f_r [GHz]	4.11	4.11	4.11
κ_{ext} [kHz]	6.8 ± 0.1	6.6 ± 0.2	6.6 ± 0.2
κ_{TLS} [kHz]	4.0 ± 0.3	5.2 ± 0.2	5.3 ± 0.2
a_c [\sqrt{n}]	1.4 ± 0.4	1.6 ± 0.4	0.51 ± 0.03
β	0.30 ± 0.02	0.3	0.133 ± 0.004

polynomial coefficients c_n . To extract the TLS damping parameters κ_{TLS} , a_c , and β from the polynomial expansion coefficients and to compare our harmonic balance results with the circle fit analysis, we perform a least-squares fitting. For this fit, we set $\kappa_0 = 0.86$ kHz, based on the value extracted from a fit of the parameters extracted from the standard circle fit to Eq. (2) in the high-power regime. This parameter can in principle be obtained from a fast frequency sweep at high power. Our reconstruction is based on measurements of a single intermodulation spectrum and encounters limitations in simultaneously capturing both a_c and β . We therefore fix $\beta = 0.3$ motivated by the slope of the third-order IMP strength in the TLS saturation regime (see Appendix E).

The resulting parameters, listed in Table II, show good agreement with the standard fit values. Without fixing the parameter β , our reconstruction method still yields the important TLS loss parameter κ_{TLS} in good agreement with the standard method. In Appendix E, we reconstruct the TLS parameters from a spectrum averaged over 1 h, obtaining results that are consistent within the error bars. Differences may be due to variable conditions across cooling cycles as the standard resonance sweeps and IMP data were obtained in separate cooldowns [39].

V. DISCUSSION AND CONCLUSION

We demonstrate the inherent nonlinear nature of parasitic TLSs in superconducting circuits by observing frequency-mixing products in a CPW resonator when driven near-resonantly by two slightly detuned drive tones. We characterize the intermodulation products of this frequency mixing as a function of drive detuning with respect to the resonance frequency, as well as the applied drive power. Drawing a comparison to the standard tunneling model for TLSs, we observe an analogous power dependence of the IMPs on applied drive power, as we expect from the conventional analysis of the Q_i suppression at

decreasing drive powers as an effect of a saturable bath of TLSs.

Repeated measurements of the IMPs generated in the device when driven by the same conditions over 25 h show correlated jumps in the IMP amplitudes. This approach provides an efficient method of studying the timescales of TLS-device interaction with a high SNR.

Using harmonic balance analysis and assuming a model for a driven harmonic oscillator with nonlinear damping, we reconstruct the nonlinear parameters of this device-TLS interaction, in good agreement with the parameters extracted from the experimental data using the conventional tunneling TLS model. Our reconstruction method is promising for characterizing TLSs in superconducting devices, as it reduces the need for a comprehensive frequency and power sweep, enabling analysis through a single intermodulation spectrum with the parameter δ_0 extracted from a fast high-power sweep. While independently determining β and a_c does require a power sweep, measuring at the single photon level is not necessary.

ACKNOWLEDGMENTS

This work was funded by the Knut and Alice Wallenberg (KAW) Foundation through the Wallenberg Center for Quantum Technology (WACQT). The device fabrication was performed at Myfab Chalmers. D.B.H. and D.F. are part owners of the company Intermodulation Products AB, which produces the digital microwave platform used in this experiment.

APPENDIX A: SAMPLE FABRICATION

The device was fabricated on a 280- μm thick, high-resistivity ($\rho \geq 10 \text{ k}\Omega \text{ cm}$), intrinsic silicon substrate. Prior to thin film deposition, the substrate was submerged in 2% HF for 60 s to remove the native surface oxide, then rinsed in deionized water and loaded immediately into a heated loadlock of a sputter deposition tool, where the substrate was heated to 80 °C during pumpdown. After

transfer into the deposition chamber, the substrate was heated to 300 °C for 10 min and left to cool down for 16 h, after which the chamber pressure was $2.2 \times 10^{-8} \text{ mbar}$. A 150 nm thick layer of Al was deposited by sputtering at 0.9 nm s^{-1} , and the film was oxidized *in situ* by static oxidation at 10 mbar.

The device was patterned by direct-write optical lithography on a poly(methylmethacrylate) (PMMA) A2 + S1805 resist stack. The optically sensitive S1805 was developed in a tetramethyl ammonium hydroxide (TMAH) based developer. After development, the exposed PMMA protecting the underlying Al from TMAH was ashed in oxygen plasma, and the pattern was transferred into Al by wet etch in an $\text{H}_3\text{PO}_4:\text{HNO}_3:\text{CH}_2\text{O}_2$ solution at room temperature.

The remaining resist was then dissolved in an *n*-methylpyrrolidone-based resist remover, acetone, and isopropanol. The wafer was coated with a fresh layer of protective photoresist (S1805), diced, and stripped again in the aforementioned solvents. The cleaning was finished with an ozone-cleaning step.

APPENDIX B: MEASUREMENT SETUP

The chip is placed in a light-tight copper sample box, where the transmission line is wire-bonded to input and output subminiature version A (SMA) connectors, and the ground plane of the CPW is wire-bonded to the copper box along the chip periphery.

The sample box is then mounted onto a copper tail attached to the mixing chamber stage of a dilution refrigerator. The copper tail is enclosed in an additional copper can coated with a layer of Stycast mixed with SiC on the inside, which is in turn enclosed in a Cryoperm magnetic shield. This is in addition to the shields attached to every temperature stage as marked in Fig. 5.

On the input signal line, the incoming signal is attenuated at each stage with individual attenuators amounting to a total of 55 dB attenuation. The input line attenuates by an

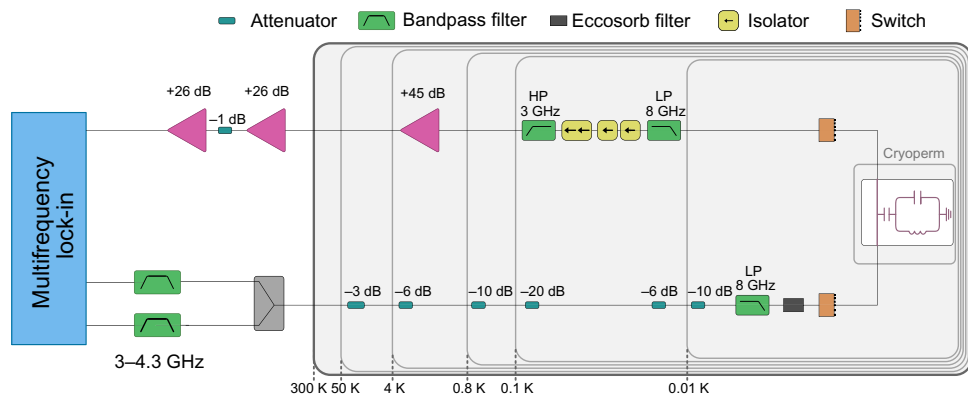


FIG. 5. Cryogenic measurement setup.

additional 11 dB at 4 GHz, as determined from an ac-Stark shift measurement of a qubit.

Microwave switches are present below the mixing chamber stage on both the input and output lines. On the output line, above the 10 mK stage, the signal is passed through a chain of microwave isolators and filters to suppress both reflected signals and thermal noise coming from the higher temperature stages and the amplifiers. The weak signal is amplified at the 4 K stage by a low-noise high electron mobility transistor cryogenic amplifier. At room temperature, the signal is further amplified by two gain block amplifiers connected in series.

For intermodulation product measurements, the cryogenic microwave measurement setup was connected to a multifrequency lock-in amplifier [22]. We use a separate signal output for each drive tone, passing through a 3–4.3-GHz bandpass filter before being combined in a power splitter and routed through the cryogenic measurement setup.

For the quality factor characterization of the device, the microwave setup was connected to a vector network analyzer, with a 30 dB attenuator added to the output of the analyzer at low power measurements.

APPENDIX C: ADDITIONAL DATA

To investigate the origins of the nonlinearity we observe through intermodulation, we repeat the intermodulation measurement; only this time, we place the frequency comb far outside the resonance, detuned by 700 kHz (Fig. 6). Here the resonator does not interact with the drive signals, and instead, we measure the transmission of our microwave measurement setup and the transmission line

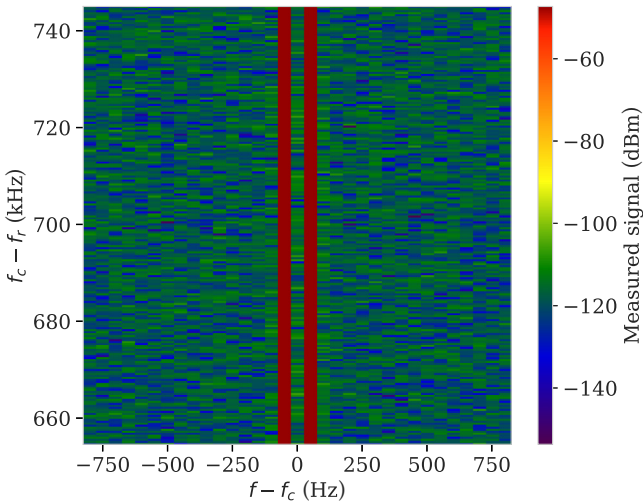


FIG. 6. Intermodulation measurement performed around a frequency 700 kHz away from resonance. We observe no intermodulation products as a result of the two drive tones, showing that the nonlinearities we observe are native to the device and not an artifact of our measurement setup.

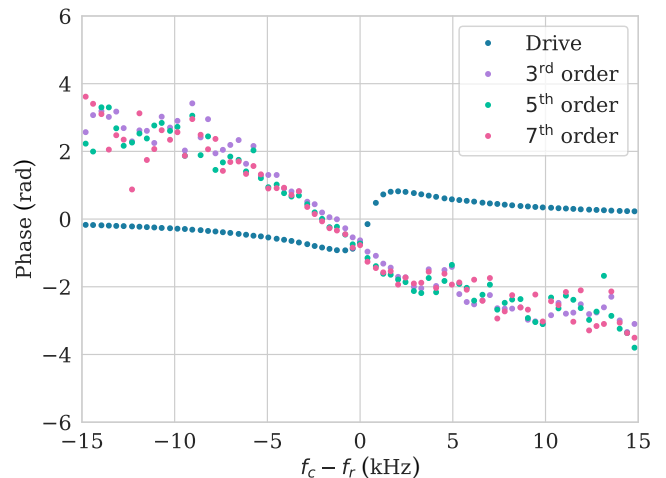


FIG. 7. The phase response of the resonator at the drive frequency and the three strongest IMPs, as a function of drive frequency. The drives are at resonance when the detection comb frequency f_c coincides with the resonance frequency f_r .

of the device itself. We do not observe any intermodulation here, ruling out the measurement setup as the origin of this nonlinearity.

We show the phase response of the resonator and the three strongest IMPs in Fig. 7. The phase response at the drive tone wraps by less than π across resonance, which is an expected response for an asymmetric, overcoupled resonator in a notch configuration [41]. The phase response of the IMPs wraps by 2π .

APPENDIX D: RESONATOR CHARACTERIZATION

The initial characterization of the resonator is performed by spectroscopy, where the complex S_{21} transmission scattering parameter is measured using a vector network analyzer. The S_{21} data are analyzed using the resonance circle

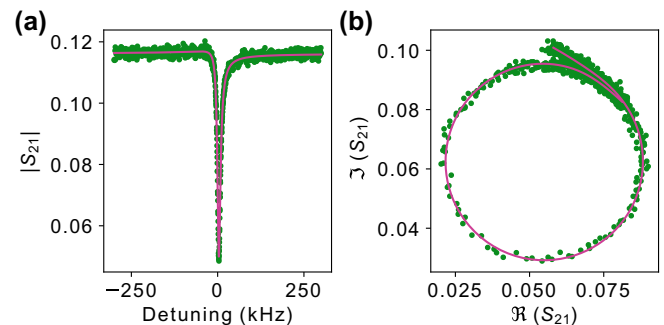


FIG. 8. The resonance circle fit method at the single photon level. (a) The fit of the absolute value of the transmission scattering parameter S_{21} as a function of frequency, with a dip in transmission at resonance. (b) The resonance circle on the complex plane.

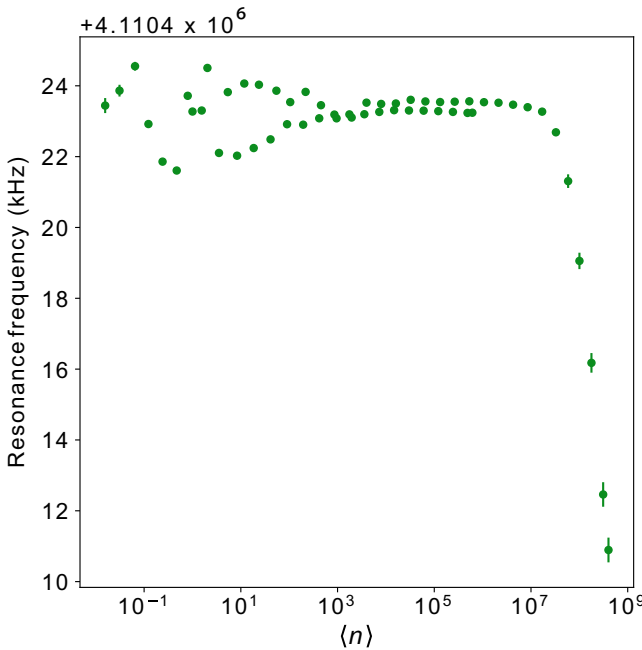


FIG. 9. The resonator's frequency extracted from a circle fit of the complex S_{21} data, as a function of average photon number $\langle n \rangle$.

fitting method with diameter correction [18]:

$$S_{21}(f) = ae^{i\alpha} e^{-2\pi f \tau} \left[1 - \frac{(Q_l/|Q_c|)e^{i\phi}}{1 + 2iQ_l(f/f_r - 1)} \right], \quad (\text{D1})$$

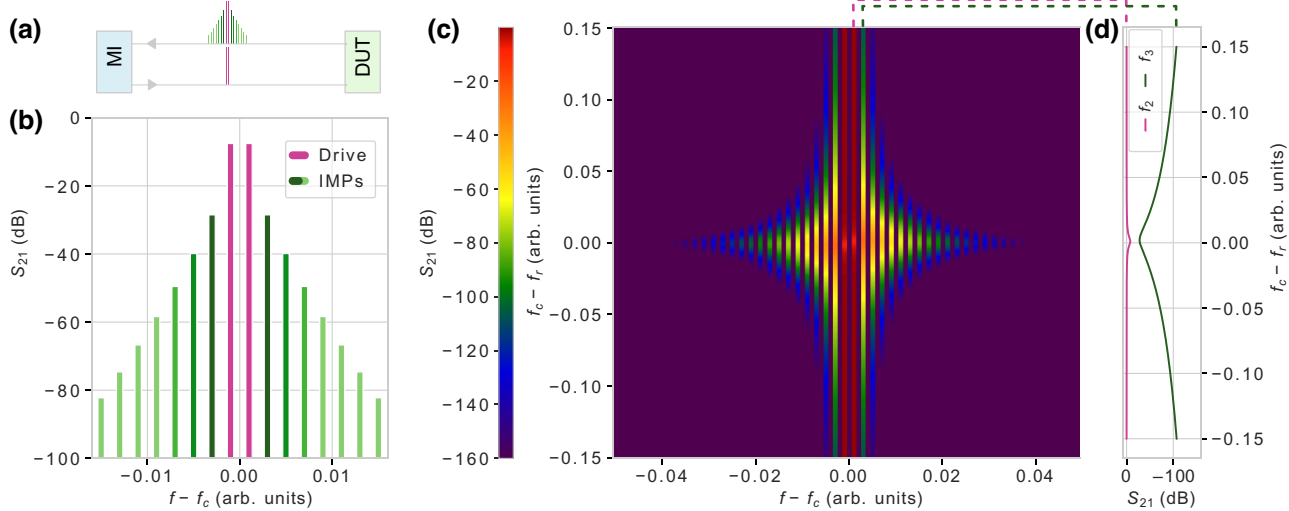


FIG. 10. Intermodulation simulation results. (a) A schematic of the input tones and the output of the device under test (DUT). (b) Simulated IMPs when two drive tones are applied inside the resonance linewidth. The abscissa shows the detection comb frequencies f relative to the center of the detection comb $f_c = (f_1 + f_2)/2$. IMPs appear at frequencies fulfilling the $f_{\text{IMP}} = k_1 f_1 + k_2 f_2$ condition, which falls on every other tone in this detection comb. (c) Simulated IMP spectroscopy performed by sweeping the frequency comb depicted in (a) across a frequency spectrum centered around the resonance frequency f_r . (d) Vertical line cuts of the simulated IMP spectroscopy data shown in (c). The device resonance shows a dip in the transmission of drive tone f_1 , and the third IMP f_3 presents a peak at $2f_2 - f_1$.

where f_r is the resonance frequency, f the probe frequency, ϕ the impedance mismatch, Q_c the coupling quality factor, and Q_l the loaded quality factor, from which Q_i can be extracted with $Q_l^{-1} = Q_i^{-1} + \text{Re}\{Q_c^{-1}\}$. The remaining parameters, additional amplitude a , phase shift α , and electronic delay τ account for environmental imperfections. For an example of the accuracy of this fit at the single photon level, see Fig. 8.

The circle fitting method is at its most reliable when the resonator is near-critically coupled to the transmission line (i.e., $Q_i \approx |Q_c|$). With a $|Q_c|$ of 6×10^5 and a Q_i in the range of 1×10^6 – 5×10^6 depending on their applied drive power, our device is close to this condition.

We show the extracted resonance frequency as a function of power in Fig. 9. The frequency shifts mirror the different regions of the Q_i vs $\langle n \rangle$ dependence seen in Fig. 2(a), where data are scattered in the low-power regime due to TLS fluctuations, and at high powers the power-dependent kinetic inductance modifies the resonance frequency and quality.

APPENDIX E: ADDITIONAL MODELING AND PARAMETER RECONSTRUCTION

We simulate a sweep of the drive frequencies across the resonance shown in Fig. 10. The drive strength presents a dip on resonance, while the IMP strength increases, qualitatively matching the experimental results in Fig. 1. We also simulate the power dependence of the third-order IMP for various β values, as illustrated in Fig. 11. Notably,

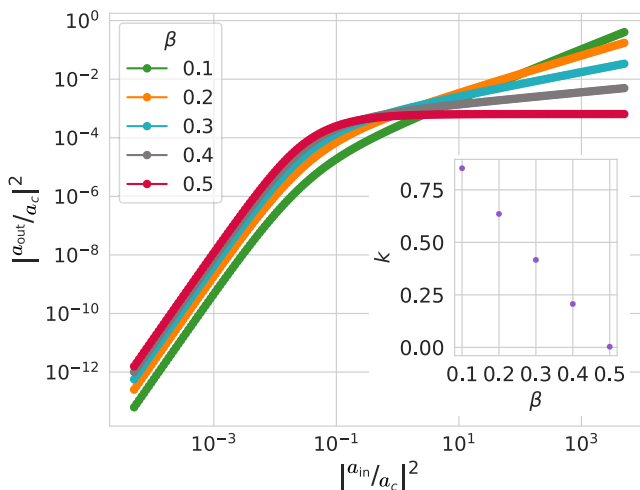


FIG. 11. Simulation of the power of the third-order IMP as a function of the input drive power normalized by photon number at different β values. The inset shows the value of the slope of the TLS saturation regime k as a function of β .

with increasing β we observe a reduction in the slope of the third-order IMP above n_c . The connection between the slope above n_c and the parameter β is seen in the inset of Fig. 11. As β increases, we observe a noticeable decrease in the slope, becoming 0 at $\beta = 0.5$. This behavior indicates that the observed power dependence above n_c is not a feature of the standard tunneling model with $\beta = 0.5$. The value of $\beta = 0.3$ found in Fig. 2 is also in agreement with this simulation.

To test the efficiency and robustness of the intermodulation spectral method combined with harmonic balance, we perform reconstructions on data acquired in 1-hour-long measurements, much shorter than what is feasible with the standard approach. The reconstructed parameters, shown in Table III, are comparable to those obtained from longer measurements, though with a slight decrease in precision. This ability to conduct rapid measurements, as opposed to the more time-consuming standard analysis, offers a significant advantage.

TABLE III. Reconstructed resonator parameters via fitting the intermodulation spectral method with harmonic balance on a 1-hour-long measurement. The confidence intervals of the reconstructed values are computed by bootstrapping.

Parameters	Harmonic balance
f_r [GHz]	4.11
κ_{ext} [kHz]	7.1 ± 0.6
κ_{TLS} [kHz]	5.7 ± 0.6
a_c [\sqrt{n}]	1.8 ± 0.3

- [1] Morten Kjaergaard, Mollie E. Schwartz, Jochen Braumüller, Philip Krantz, Joel I.-J. Wang, Simon Gustavsson, and William D. Oliver, Superconducting qubits: Current state of play, *Annu. Rev. Condens. Matter Phys.* **11**, 369 (2020).
- [2] Alexander P. M. Place *et al.*, New material platform for superconducting transmon qubits with coherence times exceeding 0.3 milliseconds, *Nat. Commun.* **12**, 1 (2021).
- [3] Peter A. Spring, Shuxiang Cao, Takahiro Tsunoda, Giulio Campanaro, Simone Fasciati, James Wills, Mustafa Bakr, Vivek Chidambaram, Boris Shteynas, Lewis Carpenter, Paul Gow, James Gates, Brian Vlastakis, and Peter J. Leek, High coherence and low cross-talk in a tileable 3D integrated superconducting circuit architecture, *Sci. Adv.* **8**, eabl6698 (2022).
- [4] Chenlu Wang *et al.*, Towards practical quantum computers: Transmon qubit with a lifetime approaching 0.5 milliseconds, *npj Quantum Inf.* **8**, 1 (2022).
- [5] A. Somoroff, Q. Ficheux, R. A. Mencia, H. Xiong, R. Kuzmin, and V. E. Manucharyan, Millisecond coherence in a superconducting qubit, *Phys. Rev. Lett.* **130**, 267001 (2023).
- [6] D. P. Pappas, M. R. Vissers, D. S. Wisbey, J. S. Kline, and J. Gao, Two level system loss in superconducting microwave resonators, *IEEE Trans. Appl. Supercond.* **21**, 871 (2011).
- [7] Jürgen Lisenfeld, Grigorij J. Grabovskij, Clemens Müller, Jared H. Cole, Georg Weiss, and Alexey V. Ustinov, Observation of directly interacting coherent two-level systems in an amorphous material, *Nat. Commun.* **6**, 6182 (2015).
- [8] Clemens Müller, Jared H. Cole, and Jürgen Lisenfeld, Towards understanding two-level-systems in amorphous solids: insights from quantum circuits, *Rep. Prog. Phys.* **82**, 124501 (2019).
- [9] M. Molina-Ruiz, Y. J. Rosen, H. C. Jacks, M. R. Abernathy, T. H. Metcalf, X. Liu, J. L. DuBois, and F. Hellman, Origin of mechanical and dielectric losses from two-level systems in amorphous silicon, *Phys. Rev. Mater.* **5**, 035601 (2021).
- [10] Sun Un, Sebastian de Graaf, Patrice Bertet, Sergey Kubatkin, and Andrey Danilov, On the nature of decoherence in quantum circuits: Revealing the structural motif of the surface radicals in α -Al₂O₃, *Sci. Adv.* **8**, eabm6169 (2022).
- [11] Martin Specker, Patrick Paluch, Nicolas Gosling, Niv Drucker, Shlomi Matityahu, Daria Gusenkova, Simon Günzler, Dennis Rieger, Ivan Takmakov, Francesco Valenti, Patrick Winkel, Richard Gebauer, Oliver Sander, Gianluigi Catelani, Alexander Shnirman, Alexey V. Ustinov, Wolfgang Werndorfer, Yonatan Cohen, and Ioan M. Pop, Two-level system hyperpolarization using a quantum Szilard engine, *Nat. Phys.* **1**, 1320 (2023).
- [12] Jeremy M. Sage, Vladimir Bolkhovsky, William D. Oliver, Benjamin Turek, and Paul B. Welander, Study of loss in superconducting coplanar waveguide resonators, *J. Appl. Phys.* **109**, 063915 (2011).
- [13] A. Megrant, C. Neill, R. Barends, B. Chiaro, Yu Chen, L. Feigl, J. Kelly, Erik Lucero, Matteo Mariantoni, P. J. J. O'Malley, D. Sank, A. Vainsencher, J. Wenner, T. C. White, Y. Yin, J. Zhao, C. J. Palmstrøm, John M. Martinis, and A. N. Cleland, Planar superconducting resonators with internal quality factors above one million, *Appl. Phys. Lett.* **100**, 113510 (2012).

- [14] Ryan Kaufman, Theodore White, Mark I. Dykman, Andrea Iorio, George Stirling, Sabrina Hong, Alex Opremcak, Andreas Bengtsson, Lara Faoro, Joseph C. Bardin, Tim Burger, Robert Gasca, and Ofer Naaman, Josephson parametric amplifier with Chebyshev gain profile and high saturation, *Phys. Rev. Appl.* **20**, 054058 (2023).
- [15] R. P. Erickson, M. R. Vissers, M. Sandberg, S. R. Jefferts, and D. P. Pappas, Frequency comb generation in superconducting resonators, *Phys. Rev. Lett.* **113**, 187002 (2014).
- [16] A. Yu. Dmitriev, R. Shaikhaidarov, T. Hönigl-Decrinis, S. E. de Graaf, V. N. Antonov, and O. V. Astafiev, Probing photon statistics of coherent states by continuous wave mixing on a two-level system, *Phys. Rev. A* **100**, 013808 (2019).
- [17] T. Weißl, S. W. Jolin, R. Borgani, D. Forchheimer, and D. B. Haviland, A general characterization method for nonlinearities in superconducting circuits, *New J. Phys.* **21**, 053018 (2019).
- [18] S. Probst, F. B. Song, P. A. Bushev, A. V. Ustinov, and M. Weides, Efficient and robust analysis of complex scattering data under noise in microwave resonators, *Rev. Sci. Instrum.* **86**, 024706 (2015).
- [19] A. Bruno, G. de Lange, S. Asaad, K. L. van der Enden, N. K. Langford, and L. DiCarlo, Reducing intrinsic loss in superconducting resonators by surface treatment and deep etching of silicon substrates, *Appl. Phys. Lett.* **106**, 182601 (2015).
- [20] D. I. Schuster, A. Wallraff, A. Blais, L. Frunzio, R.-S. Huang, J. Majer, S. M. Girvin, and R. J. Schoelkopf, ac Stark shift and dephasing of a superconducting qubit strongly coupled to a cavity field, *Phys. Rev. Lett.* **94**, 123602 (2005).
- [21] C. S. Macklin, Quantum feedback and traveling-wave parametric amplification in superconducting circuits, Ph.D. thesis, UC Berkeley, 2015.
- [22] Mats O. Tholén, Riccardo Borgani, Giuseppe Ruggero Di Carlo, Andreas Bengtsson, Christian Križan, Marina Kudra, Giovanna Tancredi, Jonas Bylander, Per Delsing, Simone Gasparinetti, and David B. Haviland, Measurement and control of a superconducting quantum processor with a fully integrated radio-frequency system on a chip, *Rev. Sci. Instrum.* **93**, 104711 (2022).
- [23] J. Burnett, L. Faoro, and T. Lindström, Analysis of high quality superconducting resonators: Consequences for tls properties in amorphous oxides, *Supercond. Sci. Tech.* **29**, 044008 (2016).
- [24] J. Burnett, J. Sagar, O. W. Kennedy, P. A. Warburton, and J. C. Fenton, Low-loss superconducting nanowire circuits using a neon focused ion beam, *Phys. Rev. Appl.* **8**, 014039 (2017).
- [25] David Nipce, Jonathan Burnett, and Jonas Bylander, High kinetic inductance NbN nanowire superconductors, *Phys. Rev. Appl.* **11**, 044014 (2019).
- [26] M. Kudra, J. Biznárová, A. Fadavi Roudsari, J. J. Burnett, D. Nipce, S. Gasparinetti, B. Wickman, and P. Delsing, High quality three-dimensional aluminum microwave cavities, *Appl. Phys. Lett.* **117**, 070601 (2020).
- [27] J. Burnett, L. Faoro, I. Wisby, V. L. Gurtovoi, A. V. Chernykh, G. M. Mikhailov, V. A. Tulin, R. Shaikhaidarov, V. Antonov, P. J. Meeson, A. Ya. Tzalenchuk, and T. Lindström, Evidence for interacting two-level systems from the 1/f noise of a superconducting resonator, *Nat. Commun.* **5**, 4119 (2014).
- [28] Lara Faoro and Lev B. Ioffe, Interacting tunneling model for two-level systems in amorphous materials and its predictions for their dephasing and noise in superconducting microresonators, *Phys. Rev. B* **91**, 014201 (2015).
- [29] Clemens Mueller, Juergen Lisenfeld, Alexander Shnirman, and Stefano Poletto, Interacting two-level defects as sources of fluctuating high-frequency noise in superconducting circuits, *Phys. Rev. B* **92**, 035442 (2015).
- [30] Hank Zumbahlen and the engineering staff Of Analog Devices, *Linear Circuit Design Handbook* (Newnes, Oxford, 2008).
- [31] L. J. Swenson, P. K. Day, B. H. Eom, H. G. Leduc, N. Llobart, C. M. McKenney, O. Noroozian, and J. Zmuidzinas, Operation of a titanium nitride superconducting microresonator detector in the nonlinear regime, *J. Appl. Phys.* **113**, 104501 (2013).
- [32] Jonas Zmuidzinas, Superconducting microresonators: Physics and applications, *Annu. Rev. Condens. Matter Phys.* **3**, 169 (2012).
- [33] Jonathan J. Burnett, Andreas Bengtsson, Marco Scigliuzzo, David Nipce, Marina Kudra, Per Delsing, and Jonas Bylander, Decoherence benchmarking of superconducting qubits, *npj Quantum Inf.* **5**, 1 (2019).
- [34] David Nipce, Jonathan J. Burnett, Marina Kudra, Jared H. Cole, and Jonas Bylander, Stability of superconducting resonators: Motional narrowing and the role of Landau-Zener driving of two-level defects, *Sci. Adv.* **7**, eabh0462 (2021).
- [35] Kimihiko Yasuda, Shozo Kawamura, and Koutaro Watanabe, Identification of nonlinear multi-degree-of-freedom systems: presentation of an identification technique, *JSME Int. J.* **31**, 8 (1988).
- [36] Carsten Hutter, Daniel Platz, E. A. Tholén, T. H. Hansson, and D. B. Haviland, Reconstructing nonlinearities with intermodulation spectroscopy, *Phys. Rev. Lett.* **104**, 050801 (2010).
- [37] Pauli Virtanen *et al.*, SciPy 1.0: Fundamental algorithms for scientific computing in Python, *Nat. Methods* **17**, 261 (2020).
- [38] Daniel Forchheimer, Daniel Platz, Erik A. Tholé, and David B. Haviland, Model-based extraction of material properties in multifrequency atomic force microscopy, *Phys. Rev. B* **85**, 195449 (2012).
- [39] Corey Rae H. McRae, Gregory M. Stiehl, Haozhi Wang, Sheng-Xiang Lin, Shane A. Caldwell, David P. Pappas, Josh Mutus, and Joshua Combes, Reproducible coherence characterization of superconducting quantum devices, *Appl. Phys. Lett.* **119**, 100501 (2021).
- [40] A. Pastore, An introduction to bootstrap for nuclear physics, *J. Phys. G: Nucl. Part. Phys.* **46**, 052001 (2019).
- [41] M. Simoen, Parametric interactions with signals and the vacuum, Ph.D. thesis, Chalmers University of Technology, 2015.